



ELSEVIER

Contents lists available at ScienceDirect

Computational Materials Science

journal homepage: www.elsevier.com/locate/commatsci



Substitutional solution of silicon in cementite: A first-principles study

Jae Hoon Jang^a, In Gee Kim^{a,*}, H.K.D.H. Bhadeshia^{a,b}

^a Graduate Institute of Ferrous Technology, Pohang University of Science and Technology, Pohang 790-784, Republic of Korea

^b Materials Science and Metallurgy, University of Cambridge, Pembroke Street, Cambridge CB2 3QZ, UK

Substitutional solution of silicon in cementite: A first-principles study

Jae Hoon Jang^a, In Gee Kim^{a,*}, H. K. D. H. Bhadeshia^{a,b}

^a*Graduate Institute of Ferrous Technology, Pohang University of Science and Technology, Pohang 790-784, Republic of Korea*

^b*Materials Science and Metallurgy, University of Cambridge, Pembroke Street, Cambridge CB2 3QZ, UK*

Abstract

Cementite precipitation from austenite in steels can be suppressed by alloying with silicon. There are, however, no validated thermodynamic data to enable phase equilibria to be estimated when silicon is present in cementite. The formation energies of Fe_3C , $(\text{Fe}_{11}\text{Si}_{\text{Fe}}^{4c})\text{C}_4$ and $(\text{Fe}_{11}\text{Si}_{\text{Fe}}^{8d})\text{C}_4$ have therefore been estimated using first-principles calculations based on the total-energy all-electron full-potential linearized augmented plane wave method within the generalized gradient approximation to density functional theory. The ground state properties such as lattice constants and bulk moduli have also been calculated. The calculations show that $(\text{Fe}_{11}\text{Si}_{\text{Fe}}^{4c})\text{C}_4$ and $(\text{Fe}_{11}\text{Si}_{\text{Fe}}^{8d})\text{C}_4$ have about $52.06 \text{ kJ mol}^{-1}$ and $37.17 \text{ kJ mol}^{-1}$ greater formation energy, respectively, than Fe_3C . The formation energy for hypothetical cementite Si_3C has also been calculated to be about 256 kJ mol^{-1} . Silicon substitution significantly reduces the magnetic moments at the Fe(4c) site for both $(\text{Fe}_{11}\text{Si}_{\text{Fe}}^{4c})\text{C}_4$ and $(\text{Fe}_{11}\text{Si}_{\text{Fe}}^{8d})\text{C}_4$, irrespective of the Si substitution sites. The calculated electronic structures indicate that the magnetic moment reduction at the Fe(4c) site by the Si substitution at 4c site is indirect through the neighboring carbon atom, whereas at the 8d site it is direct.

1 Introduction

There is a particular combination of phases in steels which has led to dramatic developments in their application in a variety of technologically vital contexts [1–13]. This combination is commonly designated *carbide-free bainite*

* Corresponding author. Tel.: +82-54-279-4409, Fax: +82-54-279-4499
Email address: igkim@postech.ac.kr (In Gee Kim).

and consists of a mixture of fine ferrite plates with a body-centred cubic (bcc) crystal structure, embedded in a matrix of carbon-enriched austenite with a face-centred cubic (fcc) structure. This latter phase is not usually stable at ambient temperatures, but is made so by preventing cementite (Fe_3C) precipitation using silicon as an alloying addition to the steel. The austenite is then able to retain carbon in solid solution, enabling it to remain untransformed to room temperature.

The specific role of silicon in suppressing cementite precipitation has been known for a long time [14–28]. For cementite to precipitate at low temperatures, it must inherit the silicon concentration of the parent phase; since the solubility of silicon in cementite is negligibly small, the trapping of silicon is thought to dramatically reduce the driving force for precipitation [29–32].

However, it has not been possible to theoretically justify the mechanism by which the silicon acts, because thermodynamic data on silicon in cementite cannot be measured due to its incredibly low solubility in the carbide. Values based on educated guesses are used in the limited calculations that exist [31,32]. The purpose of the work presented here was specifically to derive the relevant thermodynamic data using total energy calculations, in particular, by using the all-electron full-potential linearized augmented plane-wave (FLAPW) method [33,34] implemented in the QMD-FLAPW package.

2 Previous Work

As seen in Fig. 1, the crystal structure of cementite is orthorhombic with space group $Pnma$ and its experimental lattice constants are known as $a = 5.0896 \text{ \AA}$, $b = 6.7443 \text{ \AA}$ and $c = 4.5248 \text{ \AA}$ [35]. Cementite has four Fe atoms taking Fe(4c) positions which are not equivalent to the Fe(8d) positions of the other eight Fe atoms, and four C atoms located at C(4c) positions [35,36].

An *ab initio* study on pure cementite using the linear muffin-tin orbital (LMTO) method has shown the magnetic moments in the ferromagnetic state to be $1.98 \mu_B$, $1.74 \mu_B$ and $-0.06 \mu_B$ for the Fe(4c), Fe(8d) and the carbon atoms, respectively; the calculated cohesive energy per atom, E_{coh} , was found to be 8.37 eV [37]. The calculated bulk modulus is found to be 235 GPa and the magnetic moment per formula unit to be $5.77 \mu_B$ using the FLAPW method implemented in the WIEN2K package [38]. The transition from the metallic ferromagnetic to paramagnetic state occurs at about 483 K [39].

The substitution of Cr into cementite has previously been investigated; the 8d iron positions were found to be the favored sites for Cr, whose presence enhances the atomic interactions in Fe_3C leading to a considerable change in

the local distribution of the electron density according to the self-consistent full-potential LMTO (FP-LMTO) method [40].

3 Computational Model and Methods

The unit cell of cementite has an experimental volume of 155.32 \AA^3 [41] and contains four formula units of Fe_3C , where four Fe atoms take 4c positions which are not equivalent to the 8d positions of the other eight Fe atoms [36], and 4C atoms locate at 4c positions. The 4c positions for Fe are linear, while the 8d positions are tri-planar.

The Si substituted Fe_3C system is simulated by an orthorhombic unit cell with the composition $(\text{Fe}_{11}\text{Si})\text{C}_4$ corresponding to a silicon content of 4.07 wt%. This concentration is only a little higher than the 2 wt% common in the carbide-free bainitic steels [1–13]. It is also reasonable to assume that a Si atom substitutes into an iron site, because the atomic radius of Si (1.18 Å) is similar to that of Fe (1.24 Å), and much larger than that of C (0.71 Å) [42]. The location of the Si atom in the 4c or 8d site is identified using superscripts: $(\text{Fe}_{11}\text{Si}_{\text{Fe}}^{4c})\text{C}_4$ and $(\text{Fe}_{11}\text{Si}_{\text{Fe}}^{8d})\text{C}_4$. The total energy calculations for the other positions of the same Wyckoff positions show essentially the same value within numerical error.

The Kohn-Sham equation was solved self-consistently in terms of the total-energy all-electron full-potential linearized augmented plane-wave (FLAPW) method [33,34] by using the generalised gradient approximation (GGA) [43] for the exchange-correlation potential. The integrations over the three dimensional Brillouin zone (3D-BZ) were performed by the tetrahedron method [44] over a $9 \times 9 \times 9$ Monkhorst-Pack mesh [45] in the 3D-BZ which corresponds to 125, 205 and 365 \mathbf{k} -points inside the irreducible wedge of 3D-BZ for Fe_3C , $(\text{Fe}_{11}\text{Si}_{\text{Fe}}^{4c})\text{C}_4$ and $(\text{Fe}_{11}\text{Si}_{\text{Fe}}^{8d})\text{C}_4$, respectively. The degree of precision was obtained by considering a plane-wave cutoff up to 21 Ry, which corresponds to about 1700 linearized augmented plane waves per each \mathbf{k} -point and spin. The wave functions, the charge densities, and the potential were expanded with $l \leq 8$ lattice harmonics inside each muffin-tin (MT) sphere with the radii of 2.04 a.u., 2.04 a.u. and 1.30 a.u. for the Fe, Si and C atoms, respectively. The density and potential in the interstitial region were depicted by using a star-function cutoff at 340 Ry. Core electrons were treated fully relativistically, while valence states were calculated scalar relativistically, without considering spin-orbit coupling [46]. Fe-3p semicore states were treated by employing the explicit orthogonalisation (XO) scheme for ensuring the orthogonality between the core and valence electrons [47]. Self-consistency was assumed when the root-mean-square distances between the input and output total charges and spin densities were less than 1.0×10^{-5} electrons/a.u.³

The equilibrium lattice constants and the corresponding internal atomic positions were obtained by four steps. We start from the experimental lattice constants and internal coordinates [35]. (1) We vary the unit cell volume (V) followed by the 3rd order total energy fitting to find out the first step equilibrium volume $V_0^{(1)}$. (2) Then, we vary b/a with the fixed volume $V_0^{(1)}$ to find out the equilibrium b/a . (3) With the constraint obtained from the steps (1) and (2), the equilibrium c/a value is obtained. (4) Based on the previously calculated equilibrium lattice variable set ($V_0^{(1)}, b/a, c/a$), we perform the volume optimization with atomic position relaxations by the 3rd order total energy fitting. This procedure greatly reduces optimization computational time, since we do not perform on the full ($V, b/a, c/a$) total energy calculation matrix with reasonable precision. The internal atomic positions are relaxed by using the total energy and force minimization scheme using the Broyden method to find the multidimensional zero [48]. We consider a relaxed structure, when the force on each atom was smaller than 1 mRy/a.u., and the position did not change more than 3×10^{-3} a.u.

Fig. 2 and Fig. 3 show the calculated total energy versus unit cell volume with the data fitted to the 3rd order polynomial, for both the nonmagnetic (NM) and ferromagnetic (FM) states of cementite, $(\text{Fe}_{11}\text{Si}_{\text{Fe}}^{4c})\text{C}_4$ and $(\text{Fe}_{11}\text{Si}_{\text{Fe}}^{8d})\text{C}_4$.

4 Results and Discussion

Table 1 shows the results of lattice parameter optimization of Fe_3C and calculated internal coordinates compared with experimental values. The calculated unit cell volume of the FM Fe_3C is about 2% smaller than the experimental data. Based on the temperature dependent experimental lattice constants [41], the extrapolation to zero temperature gives a lattice volume of 154.4 \AA^3 , which is only about 1.4% larger than that calculated.

Tables 2, 3 and 4 contains the calculation results of equilibrium internal coordinates of Fe_3C , $(\text{Fe}_{11}\text{Si}_{\text{Fe}}^{4c})\text{C}_4$ and $(\text{Fe}_{11}\text{Si}_{\text{Fe}}^{8d})\text{C}_4$ with the distance of each atom from one of 4c and 8d position. The calculated shortest interatomic distances of Fe(8d), Fe(4c) and C(4c) from Fe(4c) are 2.495 Å, 2.695 Å and 2.015 Å in Fe_3C , respectively, which are changed to 2.466 Å, 2.669 Å and 2.061 Å, respectively, in $(\text{Fe}_{11}\text{Si}_{\text{Fe}}^{4c})\text{C}_4$. In other words, the interatomic distances of Fe(8d) and Fe(4c) measured from Si(4c) are contracted 1.2% and 1.0%, respectively, while the distance from C(4c) is expanded 2.3%. The shortest interatomic distances of Fe(8d), Fe(4c) and C(4c) measured from Fe(8d) are calculated to be 2.452 Å, 2.495 Å, and 2.011 Å in Fe_3C , respectively, which are changed to 2.421 Å, 2.466 Å and 2.175 Å in $(\text{Fe}_{11}\text{Si}_{\text{Fe}}^{8d})\text{C}_4$. This feature means that the interatomic distances from Fe(8d) to Fe(8d) and Fe(4c) are contracted 1.3% and 1.2%, respectively, while the interatomic distance to C(4c) is expanded

8.2%. These features reveal a general tendency that the substituted silicon atom pulls the neighboring iron atoms, whereas it pushes out the neighboring carbon atoms. In addition, the amounts of geometry distortions in $(\text{Fe}_{11}\text{Si}_{\text{Fe}}^{8d})\text{C}_4$ is significantly larger than those in $(\text{Fe}_{11}\text{Si}_{\text{Fe}}^{4c})\text{C}_4$ case.

Table 5 contains the energy minima of referenced elemental states and Table 6 gives the corresponding equilibrium lattice volumes, the formation energy and calculated bulk moduli of Fe_3C , $(\text{Fe}_{11}\text{Si}_{\text{Fe}}^{4c})\text{C}_4$ and $(\text{Fe}_{11}\text{Si}_{\text{Fe}}^{8d})\text{C}_4$ for the NM and FM cases. Silicon substitution increases the NM cell volume but has the opposite effect on the FM cementite. Substitution of Si in the 8d positions leads to slightly bigger cell volumes than when iron is replaced in the 4c positions on the FM cementite. The calculated bulk moduli of Fe_3C are 319.70 GPa and 226.84 GPa for the NM and FM cases, respectively. The bulk modulus of the FM case agrees reasonably with the previous first-principles result of 235.13 GPa of the FM Fe_3C cementite by Faraoun *et al.* [38] The small discrepancy is attributed to the different precision criteria they used. The calculated bulk moduli of the NM cases are about 40% higher than those of the FM cases for Fe_3C , $(\text{Fe}_{11}\text{Si}_{\text{Fe}}^{4c})\text{C}_4$ and $(\text{Fe}_{11}\text{Si}_{\text{Fe}}^{8d})\text{C}_4$. The substitution of Si into the Fe(4c) site and Fe(8d) sites reduces the bulk moduli about 4.4% and 3.2% in the NM cases, respectively. The corresponding reductions in the FM cases are about 2.2% for the 4c substitution and 2.6% for the the 8d substitution. These features indicate that the Si substitution at Fe(8d) positions leads to a larger reduction in the bulk modulus than that at the Fe(4c) positions.

The formation energies were calculated as the differences between the total energy of each phase and the sum of the energies of the stable state of pure elements forming this phase. The calculated total energies of the pure elements are summarized in Table 5. The formation energy (ΔU) of each system is defined, with the integers l , m and n , at zero Kelvin, as follows:

$$\Delta U = E(\text{Fe}_l\text{Si}_m\text{C}_n) - lE(\text{Fe}) - mE(\text{Si}) - nE(\text{C}), \quad (1)$$

where $E(\text{Fe}_l\text{Si}_m\text{C}_n)$, $E(\text{Fe})$, $E(\text{Si})$ and $E(\text{C})$ are the total energies of $\text{Fe}_l\text{Si}_m\text{C}_n$, FM bcc iron, diamond silicon and graphite carbon, respectively, at the corresponding equilibrium lattice constants. The bulk modulus of 3D symmetric crystal structure such as bcc iron and diamond silicon are calculated using the 3rd order total energy polynomial depend on lattice volume. But graphite carbon is hexagonal and the elastic modulus in c -direction is significantly smaller compared with the other axes. So the bulk modulus of hexagonal graphite should be calculated using elastic constants [49]. The 25 distinct combinations of the hexagonal lattice parameters a and c are used to determine the second order two dimensional fitting polynomial for graphite internal energy. The elastic constants ($C_{11}+C_{22}$), C_{33} , C_{13} and bulk modulus of graphite carbon are calculated to be 1248.3 GPa, 40.9 GPa, -5.7 GPa and 37.69 GPa, respectively.

The formation energy of Fe_3C is calculated to be about 21.5 kJ mol^{-1} which is only 3.2 kJ mol^{-1} larger than the experimental value, 18.3 kJ mol^{-1} [50]. The formation energies of $(\text{Fe}_{11}\text{Si}_{\text{Fe}}^{4c})\text{C}_4$ and $(\text{Fe}_{11}\text{Si}_{\text{Fe}}^{8d})\text{C}_4$ are calculated to be $138.11 \text{ kJ mol}^{-1}$ and $123.22 \text{ kJ mol}^{-1}$, respectively, which are $52.06 \text{ kJ mol}^{-1}$ and $37.17 \text{ kJ mol}^{-1}$ larger than the formation energy of four formula units of Fe_3C . It follows that 4.07 wt% silicon dissolved in a mole of cementite at zero Kelvin, requires 4.3 kJ for the 4c substitution and 3.1 kJ for the 8d substitution more energy than that required to form cementite using a mole of iron. It clearly is more difficult to form $(\text{Fe}_{11}\text{Si}_{\text{Fe}}^{4c})\text{C}_4$ and $(\text{Fe}_{11}\text{Si}_{\text{Fe}}^{8d})\text{C}_4$ than a mechanical mixture of Fe_3C and Si.

Table 7 contains the calculated results of equilibrium lattice parameters and internal coordinate of Si_3C , which is composed of the silicon atoms by replacing all the iron atoms in cementite. Compared to those values of Fe_3C , the **b**-axis of Si_3C enlarges much, so the total volume becomes 208.29 \AA^3 , which is 34.1 % larger volume than Fe_3C . The calculated formation energy of the hypothetical Si_3C cementite are $256.4 \text{ kJ mol}^{-1}$ or $1025.63 \text{ kJ (unit cell mol)}^{-1}$ for its NM calculated equilibrium lattice constants using the same optimisation procedure with Fe_3C . The calculated excess energy of the Si_3C over Fe_3C very well agree with 250 kJ mol^{-1} usually assumed in thermodynamic calculations [32,31] and 260 kJ mol^{-1} calculated using VASP [50] within 5 % error. These values are one order larger than the formation energies of Fe_3C and $\text{Fe}_{11}\text{Si}_{\text{Fe}}\text{C}_4$. When a silicon atom replaces an Fe atom in the FM cementite, the required additional formation energy is $37.17 \text{ kJ mol}^{-1}$ for the 8d sites or $52.06 \text{ kJ mol}^{-1}$ for the 4c sites. If we scale this excess energy in proportion to the corresponding site occupation numbers of iron atoms substituted with silicon in the cementite unit cell, we get $505.6 \text{ kJ (unit cell mol)}^{-1}$, which is still about half the value of the four formula unit of Si_3C . It follows that a simple analysis in terms of pairwise Si-Fe binding energies is likely to be a gross approximation of the actual effect of silicon substitution.

Fig. 4 shows the dependency of formation energy at zero Kelvin with respect to silicon concentration in cementite for the ferromagnetic cases. It is clear to see that the formation energy behavior is nonlinear to the silicon concentrations in cementite. This feature implies, in Fe_3C cementite, that more substitutional Si atoms require more formation energy in cementite.

Table 8 summarizes the calculated total magnetic moments, in units of μ_B , per formula unit, which are $5.764 \mu_B$, $4.907 \mu_B$ and $4.767 \mu_B$ for Fe_3C , $(\text{Fe}_{11}\text{Si}_{\text{Fe}}^{4c})\text{C}_4$ and $(\text{Fe}_{11}\text{Si}_{\text{Fe}}^{8d})\text{C}_4$, respectively. For Fe_3C , the calculated spin magnetic moment inside the MT spheres of Fe(8d) and Fe(4c) sites are $2.059 \mu_B$ and $1.957 \mu_B$, respectively. On the other hand, the carbon atom spins are polarized negatively to have the magnetic moment of $-0.089 \mu_B$ and the interstitial regions have a magnetic moment of $-0.479 \mu_B$.

For the case of $(\text{Fe}_{11}\text{Si}_{\text{Fe}}^{4c})\text{C}_4$, the calculated spin magnetic moments of Fe(4c), Fe(8d), C(4c), Si and interstitial region are $2.021 \mu_B$, $1.793 \mu_B$, $-0.075 \mu_B$, $-0.055 \mu_B$ and $-0.426 \mu_B$, respectively. For the case of $(\text{Fe}_{11}\text{Si}_{\text{Fe}}^{8d})\text{C}_4$, the calculated spin magnetic moment of Fe(8d), Fe(4c), C(4c) and silicon atoms and interstitial region are $1.881 \mu_B$, $1.852 \mu_B$, $-0.077 \mu_B$, $-0.076 \mu_B$ and $-1.037 \mu_B$, respectively. It is noticeable that the calculated magnetic moments of Fe(4c) atoms are reduced significantly compared with those of Fe(8d) atoms in $(\text{Fe}_{11}\text{Si}_{\text{Fe}}^{8d})\text{C}_4$, whereas the tendency of $(\text{Fe}_{11}\text{Si}_{\text{Fe}}^{8d})\text{C}_4$ case is opposite.

Fig. 5 presents the spin density contour plots in the plane normal to the **b**-axis intersect the 4c positions, whereas Fig. 6 intersect the Fe(8d) positions. The contours start from 1.0×10^{-3} electrons/a.u.³ and increase successively by a factor of $\sqrt{2}$. The solid and broken lines represent the positively and negatively polarized spins, respectively. The Si substitution on one Fe(4c) site replaces the bonding between the Fe-d and the C-sp states by that of the Si-sp and C-sp. It is noticeable that the spins of the Si-C bonding region are polarized positively, while the Fe(8d) sites are not significantly affected. In addition, the σ -like bonding between the Fe(4c)-d and the C(4c)-p shows enhanced negative spin polarization, so the positively spin polarized region of Fe(4c) site is reduced. This indirect effect of Si substitution is considered to cause the large reduction of the magnetic moment of Fe(4c) in $(\text{Fe}_{11}\text{Si}_{\text{Fe}}^{4c})\text{C}_4$.

On the other hand, the effects on the magnetism of the Si substitution on the Fe(8d) site seems rather direct. Fig. 7 presents the spin density contour plots in the plane which contains Fe(4c), C(4c), and Fe(8d) sites simultaneously for (a) Fe_3C and (b) $(\text{Fe}_{11}\text{Si}_{\text{Fe}}^{8d})\text{C}_4$ by replacing one Fe(8d) atom by Si(8d), respectively. The Si substitution on Fe(8d) site brings up the positive spin polarization on the C-Si bonding region as seen in the case of $\text{Fe}_{11}\text{Si}_{\text{Fe}}^{4c}\text{C}_4$ in Fig. 5 and Fig. 6. However, the spins of the π -like bonding between Si(8d)-p and Fe(4c)-d are polarized negatively due to the Si substitution. It is considered that the magnetic moment reduction on the Fe(4c) site by Si substitution on Fe(8d) site is due to the direct effect of the π -like bonding between the Si(8d)-p and the Fe(4c)-d states.

In Fig. 8, we present the calculated atom projected local density of states (LDOS) for the (a) Fe(4c) and (b) Fe(8d) atoms. The solid lines, broken lines, and dot-dashed lines represent the atoms belonging to Fe_3C , $(\text{Fe}_{11}\text{Si}_{\text{Fe}}^{4c})\text{C}_4$, and $(\text{Fe}_{11}\text{Si}_{\text{Fe}}^{8d})\text{C}_4$, respectively. The spin down DOS values are factored by -1 , and the Fermi levels (E_F) are set to zero. We find that all the Fe bands are broadened and split into sub-bands by the silicon substitution, due to local symmetry breaking caused by the substitution. This feature is considered to be the reason for the general reduction of Fe magnetic moments by the silicon substitutions. Compared to the band structure for Fe_3C , the sub-band splitting of Fe(4c) happens for all the silicon substitution cases. On the other hand, the Fe(8d) spin-up band peak at -0.8 eV is shifted to -1.6 eV for the case of 8d

substitution. These features agree well with the indirect effects of Fe(4c) sites and the direct effects of Fe(8d) sites by the Fe-C-Fe bond distortions due to silicon substitutions, as seen in Figs. 5, 6 and 7.

5 Conclusions

The electronic structures and magnetic properties of cementite Fe_3C and its corresponding silicon substituted forms $(\text{Fe}_{11}\text{Si}_{\text{Fe}}^{4c})\text{C}_4$, $(\text{Fe}_{11}\text{Si}_{\text{Fe}}^{8d})\text{C}_4$ and Si_3C have been investigated using first-principles calculations based on the FLAPW method within the GGA. The bulk modulus of Fe_3C is reduced a few percent on substitution of Si. The calculated equilibrium volume of ferromagnetic Fe_3C at the ground state agrees well (within 1.4%) with the experimental data extrapolated to zero Kelvin. The internal coordinate relaxations show that the substituted Si atom pulls the neighboring Fe atoms, while it pushes the neighboring carbon atoms.

The total energy calculations indicate that the Si substitution of an individual silicon atom in cementite leads to about $52.06 \text{ kJ mol}^{-1}$ for the Si(4c) substitutions or $37.17 \text{ kJ mol}^{-1}$ for the Si(8d) substitutions increment in the formation energy. The corresponding excess energy when all the iron atoms are substituted to form Si_3C is 78.3 kJ per one mole of silicon. A simple analysis in terms of pairwise Si-Fe binding energies is likely to be a gross approximation of the actual effect of silicon substitution.

It is found that on substitution of a silicon atom, the magnetic moment of the Fe(4c) site is reduced more than that of the Fe(8d) site. The calculated spin density contour plots and the Fe(4c) projected LDOS reveal that the magnetic moment reduction at Fe(4c) site by the Si substitution at 4c site is indirect bonding through the neighboring carbon atom, whereas at the 8d site it is direct.

Acknowledgements

The authors are grateful to Professor Hae-Geon Lee for the provision of laboratory facilities at the Graduate Institute of Ferrous Technology (GIFT), POSTECH.

References

- [1] O. Matsumura, Y. Sakuma, H. Takechi, Enhancement of elongation by retained austenite in intercritically annealed 0.4C-1.5Si-0.8Mn Steel: Transactions of the Iron and Steel Institute of Japan 27 (1987) 570–579.
- [2] O. Matsumura, Y. Sakuma, H. Takechi, TRIP and its kinetic aspects in austempered 0.4C-1.5Si-0.8Mn steel: Scripta Metallurgica 27 (1987) 1301–1306.
- [3] F. G. Caballero, H. K. D. H. Bhadeshia, K. J. A. Mawella, D. G. Jones, P. Brown, Design of novel high strength bainitic steels, Part1: Materials Science and Technology 17 (2001) 512–516.
- [4] F. G. Caballero, H. K. D. H. Bhadeshia, K. J. A. Mawella, D. G. Jones, P. Brown, Design of novel high strength bainitic steels, Part2: Materials Science and Technology 17 (2001) 517–522.
- [5] F. G. Caballero, H. K. D. H. Bhadeshia, K. J. A. Mawella, D. G. Jones, P. Brown, Very strong low temperature bainite: Materials Science and Technology 18 (2002) 279–284.
- [6] C. Garcia-Mateo, F. G. Caballero, H. K. D. H. Bhadeshia, Development of hard bainite: ISIJ International 43 (2003) 1238–1243.
- [7] C. Garcia-Mateo, F. G. Caballero, H. K. D. H. Bhadeshia, Acceleration of low-temperature bainite: ISIJ International 43 (2003) 1821–1825.
- [8] J. G. Speer, D. V. Edmonds, F. C. Rizzo, D. K. Matlock, Partitioning of carbon from supersaturated plates of ferrite, with application to steel processing and fundamentals of the bainite transformation: Current Opinion in Solid State and Materials Science 8 (2004) 219–237.
- [9] F. G. Caballero, H. K. D. H. Bhadeshia, Very strong bainite: Current Opinion in Solid State and Materials Science 8 (2004) 251–257.
- [10] P. J. Jacques, Transformation-induced plasticity for high strength formable steels: Current Opinion in Solid State and Materials Science 8 (2004) 259–265.
- [11] Z. G. Yang, H. S. Fang, An overview on bainite formation in steels: Current Opinion in Solid State and Materials Science 9 (2005) 277–286.
- [12] B. De Cooman, Structure-properties relationship in TRIP steels containing carbide-free bainite: Current Opinion in Solid State and Materials Science 8 (2004) 285–303.
- [13] S. Chatterjee, M. Muruganath, H. K. D. H. Bhadeshia, δ -TRIP steel: Materials Science and Technology 23 (2007) 819–827.
- [14] E. C. Bain, Alloying Elements in Steel: American Society of Materials, Cleveland, Ohio, USA, 1939.
- [15] A. G. Allen, P. Payson, The Effect of Silicon on the Tempering of Martensite: Trans. ASM 45 (1953) 498–532.

- [16] W. S. Owen, The effect of silicon on the kinetics of tempering: *Trans. ASM* 46 (1954) 812–829.
- [17] S. J. Matas, R. F. Hehemann, The structure of bainite in hypoeutectoid steels: *TMS–AIME* 221 (1961) 179–185.
- [18] R. Entin: The elementary reactions in the austenite→pearlite, bainite transformations: in: V. F. Zacky, H. I. Aaronson (Eds.), *Decomposition of austenite by diffusional processes*: Interscience, New York, 1962: pp. 295–211.
- [19] A. S. Keh, W. C. Leslie: *Structure and properties of engineering materials*: in: *Materials Science Research*: Vol. 1: Plenum Publishing, N. Y. USA, 1963.
- [20] J. Deliry, A new iron carbide during bainitic transformation in silicon-carbon steels: *Memoires Scientifiques Rev. Metallurg.* 62 (1965) 527–550.
- [21] J. Pomey, Revenu de la martensite et reaction bainitique inferieure — cas des aciers au carbone-silicium et des aciers au carbone: *Memoires Scientifiques Rev. Metallurg.* 63 (1966) 507–532.
- [22] J. Gordine, I. Codd, The influence of silicon up to 1.5 wt.percent on the tempering characteristics of a spring steel: *Journal of the Iron and Steel Institute* 207 (1969) 461–467.
- [23] R. F. Hehemann: The bainite transformation: in: H. I. Aaronson, V. F. Zackay (Eds.), *Phase Transformations*: 1970: pp. 397–432.
- [24] R. Le-Houillier, G. Begin, A. Dubé, A study of the peculiarities of austenite during the bainite transformation: *Metallurgical Transactions* 2 (1971) 2645–2653.
- [25] G. W. Lorimer, R. M. Hobbs, N. Ridley, Effect of Si on the Microstructure of quenched and tempered medium-C steels: *Journal of the Iron and Steel Institute* 210 (1972) 757–764.
- [26] B. J. P. Sandvik, The bainite reaction in Fe-Si-C alloys, the primary stage: *Metallurgical Transactions* 13A (1982) 777–787.
- [27] B. J. P. Sandvik, The bainite reaction in Fe-Si-C alloys, the secondary stage: *Metallurgical & Materials Transactions A* 13A (1982) 789–800.
- [28] H. K. D. H. Bhadeshia, D. V. Edmonds, Bainite in silicon steels: new composition–property approach Part 1: *Metal Science* 17 (1983) 420–425.
- [29] H. K. D. H. Bhadeshia, Advances in the kinetic theory of carbide precipitation: *Materials Science Forum* 426–432 (2003) 35–42.
- [30] H. K. D. H. Bhadeshia, M. Lord, L.-E. Svensson, Silicon–Rich Bainite Steel Welds: *Transactions of JWRI* 32 (2003) 43–52.
- [31] G. Ghosh, G. B. Olson, Precipitation of paraequilibrium cementite: Experiments, and thermodynamic and kinetic modeling: *Acta Materialia* 50 (2002) 2099–2119.

- [32] E. Kozeschnik, H. K. D. H. Bhadeshia, Influence of silicon on cementite precipitation in steels: *Materials Science and Technology* 24 (2008) DOI: 10.1179/174328408X275973.
- [33] E. Wimmer, H. Krakauer, M. Weinert, A. J. Freeman, Full potential self-consistent linearized augmented plane wave method for calculating the electronic structure of molecules and surfaces: O₂ molecule: *Physical Review B* 24 (1981) 864–875.
- [34] M. Weinert, E. Wimmer, and A. J. Freeman, Total-energy all-electron density functional method for bulk solids and surfaces: *Physical Review B* 26 (1982) 4571–4578.
- [35] E. J. Fasiska, G. A. Jeffrey, On the cementite Structure: *Acta Crystallographica* 19 (1965) 463–471.
- [36] F. H. Herbst, J. Smuts, Comparison of X-ray and neutron-diffraction refinements of the structure of cementite Fe₃C: *Acta Crystallographica* 17 (1964) 1331–1332.
- [37] J. Häglund, G. Grimvall, T. Jarlborg, Electronic structure, X-ray photoemission spectra, and transport properties of Fe₃C (cementite): *Physical Review B* 44 (1991) 2914–2919.
- [38] H. I. Faraoun, Y. D. Zhang, C. Esling, H. Aourag, Crystalline, electronic, and magnetic structures of θ -Fe₃C, χ -Fe₅C₂, η -Fe₂C from first principle calculations: *Journal of Applied Physics* 99 (2006) 093508.
- [39] A. Tsuzuki, S. Sago, S. I. Hirano, S. Naka, High temperature and pressure preparation and properties of iron carbides Fe₇C₃ and Fe₃C: *Journal of Materials Science* 19 (1984) 2513–2518.
- [40] N. I. Medvedeva, L. E. Kar’kina, A. L. Ivanovskii, Effect of chromium on the electronic structure of the cementite Fe₃C: *Physics of the Solid State* 48 (2006) 15–19.
- [41] I. G. Wood, L. V. cadlo, K. S. Knight, D. P. Dobson, W. G. Marshall, G. D. Price, J. Brodholt, Thermal expansion and crystal structure of cementite, Fe₃C, between 4 and 600 K determined by time-of-flight neutron powder diffraction: *Journal of Applied Crystallography* 37 (2004) 82–90.
- [42] W. D. C. Jr.: *Materials Science and Engineering: An Introduction*: Wiley, 2003.
- [43] J. P. Perdew, K. Burke, M. Ernzerhof, Generalized gradient approximation made simple: *Physical Review Letters* 77 (1996) 3865–3868.
- [44] J. Rath, A. J. Freeman, Generalized magnetic susceptibilities in metals, application of the analytic tetrahedron linear energy method to Sc: *Physical Review B* 11 (1975) 2109–2117.
- [45] H. J. Monkhorst, J. D. Pack, Special points for Brillouin-zone integrations: *Physical Review B* 13 (1976) 5188–5192.

- [46] D. D. Koelling, B. N. Harmon, A technique for relativistic spin-polarised calculations: *Journal of Physics C* 10 (1977) 3107–3114.
- [47] M. Weinert, I. G. Kim, J.H. Song, A. J. Freeman: Unpublished work (2008).
- [48] W. Mannstadt, A. J. Freeman, Dynamical and geometrical aspects of NO chemisorption on transition metals: Rh, Pd, and Pt: *Physical Review B* 55 (1997) 13 298–13 303.
- [49] J. C. Boettger, All-electron full-potential calculation of the electronic band structure, elastic constants, and equation of state for graphite: *Physical Review B* 55 (1997) 11 202–11 211.
- [50] G. Miyamoto , J.C. Oh , K. Hono , T. Furuhashi , T. Maki, Effect of partitioning of Mn and Si on the growth kinetics of cementite in tempered Fe-0.6 mass% C martensite: *Acta Materialia* 55 (2007) 5027–5038.
- [51] <http://www.webelements.com/>

Table 1. Calculated equilibrium lattice parameters (in units of \AA), unit cell volume (in units of \AA^3) and internal coordinates (in fractional units) of the Fe_3C cementite crystal structure. The experimental values of the cementite crystal structure are included as reference.

Table 2. Calculated atomic positions (in fractional units) of Fe_3C . $d(4c)$ and $d(8d)$ are the calculated interatomic distances in units of \AA measured from one of $\text{Fe}(4c)$ and $\text{Fe}(8d)$, respectively.

Table 3. Calculated atomic positions (in fractional unit) of $(\text{Fe}_{11}\text{Si}_{\text{Fe}}^{4c})\text{C}_4$. $d(\text{Si})$ is the interatomic distance in units of \AA measured from the $\text{Si}(4c)$ atom which replaces $\text{Fe}(4c)$.

Table 4. Calculated atomic positions (in fractional units) of $(\text{Fe}_{11}\text{Si}_{\text{Fe}}^{8d})\text{C}_4$. $d(\text{Si})$ is the distance in units of \AA measured from the $\text{Si}(8d)$ which replaces $\text{Fe}(8d)$.

Table 5. Calculated equilibrium unit cell volumes, total energies, and bulk moduli of the reference materials of bcc Fe, graphite C and diamond Si. The experimental bulk moduli of the pure elements as included for reference, V_0 is the experimental volumes of the unit cells of the reference elements.

Table 6. Equilibrium unit cell volume, formation energy, and bulk moduli in nonmagnetic(NM) and ferromagnetic(FM) cases, which are calculated using the 3rd order polynomial fitting with $V_0 = 155.32 \text{\AA}^3$, the experimental volume of Fe_3C . The bulk modulus of carbon is calculated using elastic constants following the method which is used in Ref. [49]. The energy is stated in units of kJ mol^{-1} of each formula unit cells. Fe_3C and Si_3C have also the formation energy which is multiplied by 4 in parentheses to compare with $\text{Fe}_{11}\text{SiC}_4$ cases.

Table 7. Calculated equilibrium lattice parameters in units of \AA and internal coordinate in fractional units of the hypothetical Si_3C with the fully optimized structure. The calculated value of the Fe_3C cementite crystal structure as included for reference.

Table 8. Calculated magnetic moments per formula unit of Fe_3C , $(\text{Fe}_{11}\text{Si}_{\text{Fe}}^{4c})\text{C}_4$ and $(\text{Fe}_{11}\text{Si}_{\text{Fe}}^{8d})\text{C}_4$ and those of each atom (in units of μ_B) inside each muffin-tin (MT) sphere and those of interstitial region.

Fig. 1. Crystal structure of cementite. The dark small spheres, the dark big spheres, and the light big spheres represent $\text{C}(4c)$, $\text{Fe}(4c)$ and $\text{Fe}(8d)$ atoms, respectively.

Fig. 2. Total energy versus unit cell volume of Fe_3C with the optimized value of b/a and c/a . The crosses represent the nonmagnetic results, while the squares represent the ferromagnetic ones with experimental internal coordinates [35]. The circles represent the ferromagnetic ones with optimized internal coordinates.

dinates. The corresponding lines are 3rd order polynomial fits. The arrows indicate the corresponding equilibrium lattice volumes.

Fig. 3. Total energy versus unit cell volume of $(\text{Fe}_{11}\text{Si}_{\text{Fe}}^{4c})\text{C}_4$ and $(\text{Fe}_{11}\text{Si}_{\text{Fe}}^{8d})\text{C}_4$ with the optimized value of b/a and c/a . The crosses represent the nonmagnetic results, while the squares represent the ferromagnetic ones with experimental internal coordinates [35]. The calculated energies of $(\text{Fe}_{11}\text{Si}_{\text{Fe}}^{4c})\text{C}_4$ is hardly distinguishable from those of $(\text{Fe}_{11}\text{Si}_{\text{Fe}}^{8d})\text{C}_4$, so only $(\text{Fe}_{11}\text{Si}_{\text{Fe}}^{4c})\text{C}_4$ case is plotted. The hollow circles and the solid circles represent the ferromagnetic ones of $(\text{Fe}_{11}\text{Si}_{\text{Fe}}^{4c})\text{C}_4$ and $(\text{Fe}_{11}\text{Si}_{\text{Fe}}^{8d})\text{C}_4$, respectively, using optimized internal coordinates. The corresponding lines are 3rd order polynomial fits. The arrows indicate the corresponding equilibrium lattice volumes.

Fig. 4. Calculated formation energy of one mole of unit cell with respect to Si concentration (in units of at%) in Fe_3C cementite. The line is drawn to guide for eyes.

Fig. 5. Spin density contour plots in the plane normal to the \mathbf{b} -axis, cutting the $4c$ plane of (a) Fe_3C and (b) $(\text{Fe}_{11}\text{Si}_{\text{Fe}}^{4c})\text{C}_4$. The horizontal axis represents $[100]$ direction, while the vertical axis represents $[001]$ one. Contours start from 1.0×10^{-3} electrons/a.u.³ and increase successively by a factor of $\sqrt{2}$. The solid and broken lines represent the positively and negatively polarized spins, respectively.

Fig. 6. Spin density contour plots in the plane normal to the \mathbf{b} -axis, cutting the $\text{Fe}(8d)$ positions of (a) Fe_3C and (b) $(\text{Fe}_{11}\text{Si}_{\text{Fe}}^{4c})\text{C}_4$. The horizontal axis represents $[100]$ direction, while the vertical axis represents $[001]$ one. Contours start from 1.0×10^{-3} electrons/a.u.³ and increase successively by a factor of $\sqrt{2}$. The solid and broken lines represent the positively and negatively polarized spins, respectively.

Fig. 7. Spin density contour plots in the plane which contains $\text{Fe}(4c)$, $\text{C}(4c)$, and $\text{Fe}(8d)$ sites simultaneously for (a) Fe_3C and (b) $(\text{Fe}_{11}\text{Si}_{\text{Fe}}^{8d})\text{C}_4$ by replacing one $\text{Fe}(8d)$ atom by $\text{Si}(8d)$, respectively. The horizontal axis represents $[100]$ direction, while the vertical axis represents $[085]$ one. Contour starts from 1.0×10^{-3} electrons/a.u.³ and increase successively by a factor of $\sqrt{2}$. The solid and broken lines represent the positively and negatively polarized spins, respectively.

Fig. 8. The calculated atom projected local density of states (LDOS) for the (a) $\text{Fe}(4c)$ and (b) $\text{Fe}(8d)$ atoms. The solid lines, broken lines, and dot-dashed lines represent the atoms belonging to Fe_3C , $(\text{Fe}_{11}\text{Si}_{\text{Fe}}^{4c})\text{C}_4$, and $(\text{Fe}_{11}\text{Si}_{\text{Fe}}^{8d})\text{C}_4$, respectively. The spin down DOS values are factored by -1 , and the Fermi levels (E_F) are set to zero.

Table 1

parameter	calculation	experiment [35]
a	5.1281 Å	5.0896 Å
b	6.6512 Å	6.7443 Å
c	4.4623 Å	4.5248 Å
volume	152.20 Å ³	155.32 Å ³
x_1	0.1752	0.1816
x_2	0.0358	0.0367
x_3	0.1236	0.1230
y_1	0.0662	0.0666
z_1	0.1670	0.1626
z_2	0.1602	0.1598
z_3	0.0621	0.0560

Table 2

type	x	y	z	$d(4c) / \text{\AA}$	$d(8d) / \text{\AA}$
Fe(8d)	0.1752	0.0662	0.3330	2.625	0.000
Fe(8d)	0.1752	0.4338	0.3330	2.625	2.452
Fe(8d)	-0.1752	-0.0662	-0.3330	2.495	3.594
Fe(8d)	-0.1752	-0.4338	-0.3330	4.753	4.823
Fe(8d)	0.3248	-0.0662	-0.1670	2.581	2.526
Fe(8d)	0.3248	-0.4338	-0.1670	4.799	4.090
Fe(8d)	-0.3248	0.0662	0.1670	2.662	2.677
Fe(8d)	-0.3248	0.4338	0.1670	2.662	3.631
Fe(4c)	-0.0358	0.2500	-0.1602	0.000	2.625
Fe(4c)	-0.0358	-0.2500	0.1602	3.650	2.495
Fe(4c)	0.4642	-0.2500	0.3398	4.582	2.581
Fe(4c)	-0.4642	0.2500	-0.3398	2.695	4.625
C(4c)	0.1236	-0.2500	-0.4379	3.589	4.053
C(4c)	-0.1236	0.2500	0.4379	2.800	2.021
C(4c)	0.3764	0.2500	0.0621	2.015	2.011
C(4c)	-0.3764	-0.2500	-0.0621	3.977	3.953

Table 3

type	x	y	z	$d(\text{Si}) / \text{\AA}$
Si(4c)	0.0301	0.2500	-0.1578	0.000
Fe(8d)	0.1780	0.0673	0.3382	2.644
Fe(8d)	0.1780	0.4327	0.3382	2.644
Fe(8d)	-0.1726	-0.0644	-0.3298	2.466
Fe(8d)	-0.1726	-0.4356	-0.3298	4.754
Fe(8d)	0.3201	-0.0646	-0.1638	2.575
Fe(8d)	0.3201	0.5646	-0.1638	2.575
Fe(8d)	-0.3214	0.0667	0.1583	2.601
Fe(8d)	-0.3214	0.4333	0.1583	2.601
Fe(4c)	-0.0368	-0.2500	0.1624	3.647
Fe(4c)	0.4682	-0.2500	0.3424	4.607
Fe(4c)	-0.4627	0.2500	-0.3442	2.669
C(4c)	0.1241	-0.2500	-0.4374	3.596
C(4c)	-0.1326	0.2500	0.4290	2.757
C(4c)	0.3818	0.2500	0.0630	2.061
C(4c)	-0.3799	-0.2500	-0.0665	3.968

Table 4

type	x	y	z	$d(\text{Si}) / \text{\AA}$
Si(8d)	0.1987	0.0627	0.3391	0.000
Fe(8d)	0.1725	0.4250	0.3314	2.421
Fe(8d)	-0.1737	-0.0727	-0.3353	3.688
Fe(8d)	-0.1811	-0.4391	-0.3320	4.904
Fe(8d)	0.3207	-0.0713	-0.1627	2.498
Fe(8d)	0.3262	-0.4375	-0.1628	4.076
Fe(8d)	-0.3192	0.0738	0.1613	2.781
Fe(8d)	-0.3233	0.4418	0.1630	3.772
Fe(4c)	0.0408	0.2432	-0.1683	2.696
Fe(4c)	-0.0326	-0.2402	0.1684	2.466
Fe(4c)	0.4587	-0.2490	0.3443	2.473
Fe(4c)	-0.4729	0.2429	-0.3549	4.799
C(4c)	0.1196	-0.2739	-0.4255	4.114
C(4c)	-0.1414	0.2710	0.4484	2.287
C(4c)	0.3825	0.2758	0.0380	2.175
C(4c)	-0.3771	-0.2512	-0.0540	4.032

Table 5

Element	Volume / \AA^3	V/V ₀	Energy / kJ mol^{-1}	Bulk Modulus / GPa	
				calculated	measured [51]
bcc Fe(FM)	11.3661	0.965	-3340575.0321	185.20	170
graphite C	8.8941	1.008	-99997.1282	37.69	33
diamond Si	20.4622	0.992	-761219.3261	88.52	100

Table 6

Type	Volume / \AA^3	V/V_0	ΔU / kJ mol^{-1}	Bulk modulus / GPa
$\text{Fe}_3\text{C}(\text{NM})$	143.27	0.922	73.9(295.63)	319.7
$(\text{Fe}_{11}\text{Si}_{\text{Fe}}^{4c})\text{C}_4(\text{NM})$	144.65	0.931	316.22	305.79
$(\text{Fe}_{11}\text{Si}_{\text{Fe}}^{8d})\text{C}_4(\text{NM})$	144.65	0.931	316.41	309.57
$\text{Fe}_3\text{C}(\text{FM})$	152.20	0.980	21.5(86.05)	226.84
$(\text{Fe}_{11}\text{Si}_{\text{Fe}}^{4c})\text{C}_4(\text{FM})$	151.44	0.975	138.11	221.83
$(\text{Fe}_{11}\text{Si}_{\text{Fe}}^{8d})\text{C}_4(\text{FM})$	151.97	0.978	123.22	221.00
$\text{Si}_3\text{C}(\text{NM})$	208.29	1.341	256.4(1025.63)	130.90

Table 7

parameter	Fe ₃ C	Si ₃ C
<i>a</i>	5.1281 Å	5.2745 Å
<i>b</i>	6.6512 Å	8.1651 Å
<i>c</i>	4.4623 Å	4.8365 Å
volume	152.20 Å ³	208.29 Å ³
<i>x</i> ₁	0.1752	0.2514
<i>x</i> ₂	0.0358	0.0109
<i>x</i> ₃	0.1236	0.2454
<i>y</i> ₁	0.0662	0.0327
<i>z</i> ₁	0.1670	0.1896
<i>z</i> ₂	0.1602	0.2558
<i>z</i> ₃	0.0621	0.0588

Table 8

region	Fe ₃ C	Fe ₃ C (LMTO)[37]	(Fe ₁₁ Si _{Fe} ^{4c})C ₄	(Fe ₁₁ Si _{Fe} ^{8d})C ₄
formula unit	5.764	-	4.907	4.767
Fe(4c)	2.059	1.98	2.021	1.881
Fe(8d)	1.957	1.74	1.793	1.852
C(4c)	-0.089	-0.06	-0.075	-0.077
Si(4c)	-	-	-0.055	-
Si(8d)	-	-	-	-0.076
interstitial	-0.120	-	-0.107	-0.259

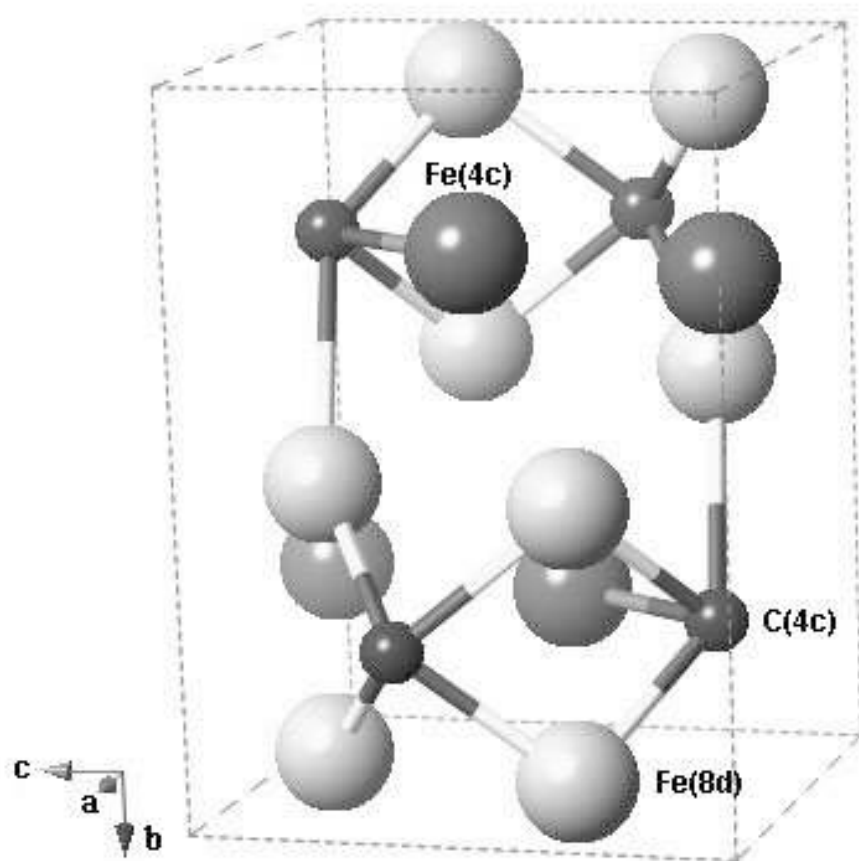


Fig. 1.

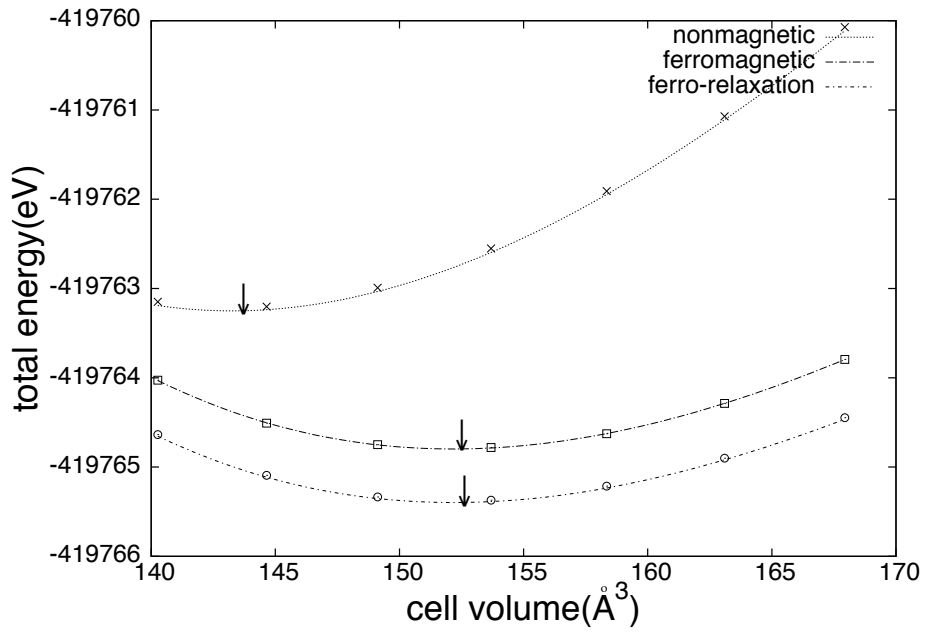


Fig. 2.

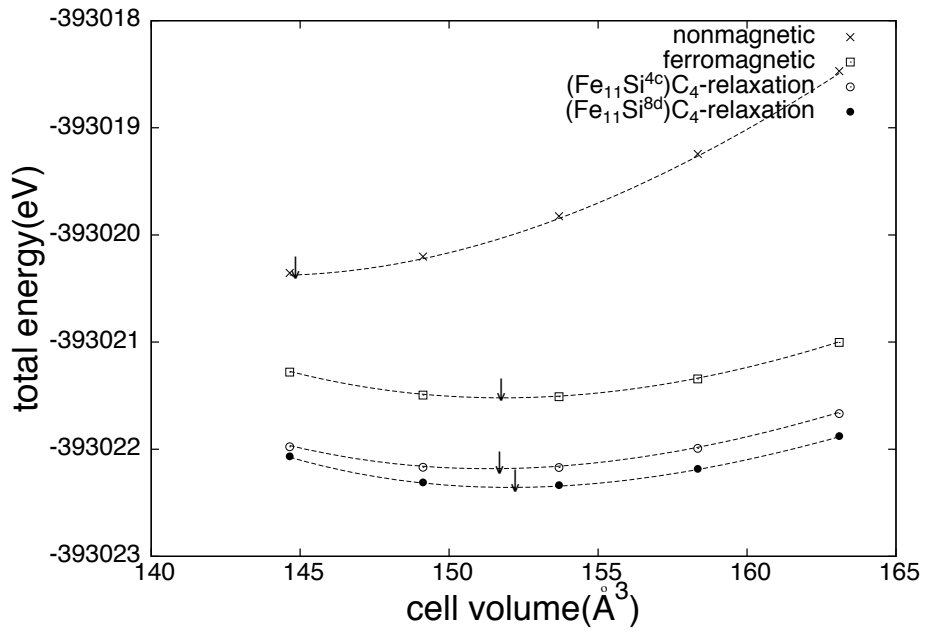


Fig. 3.

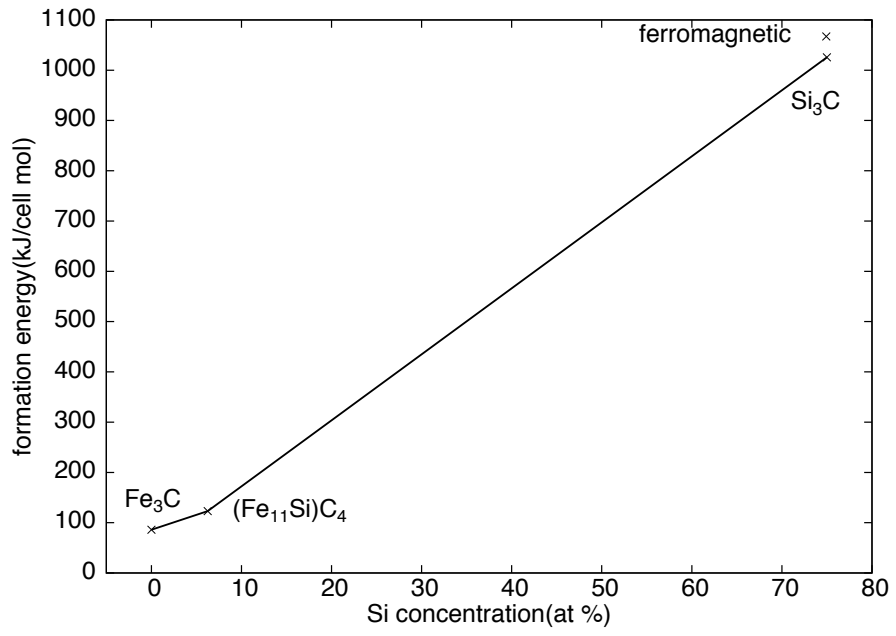


Fig. 4.

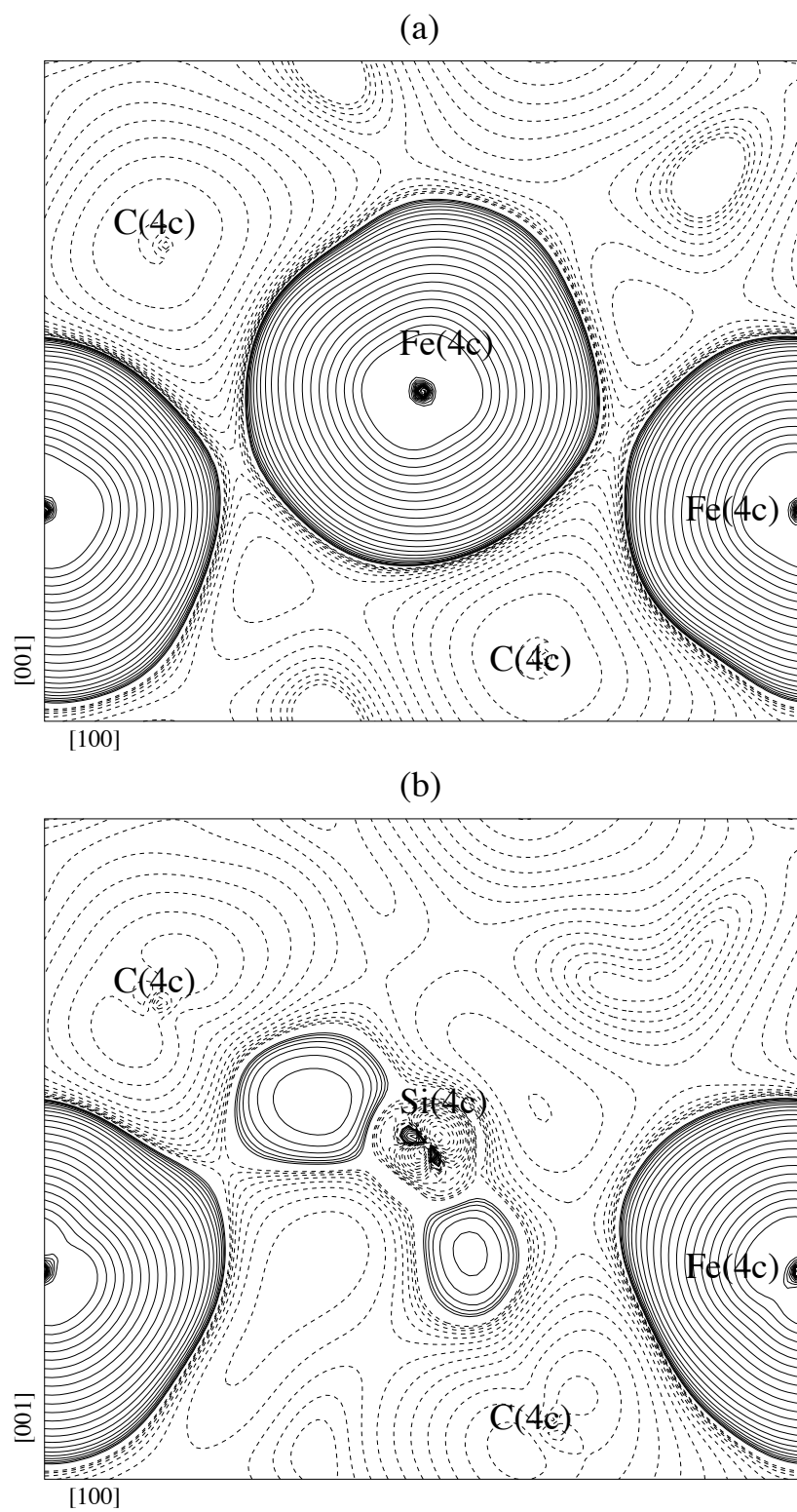


Fig. 5.

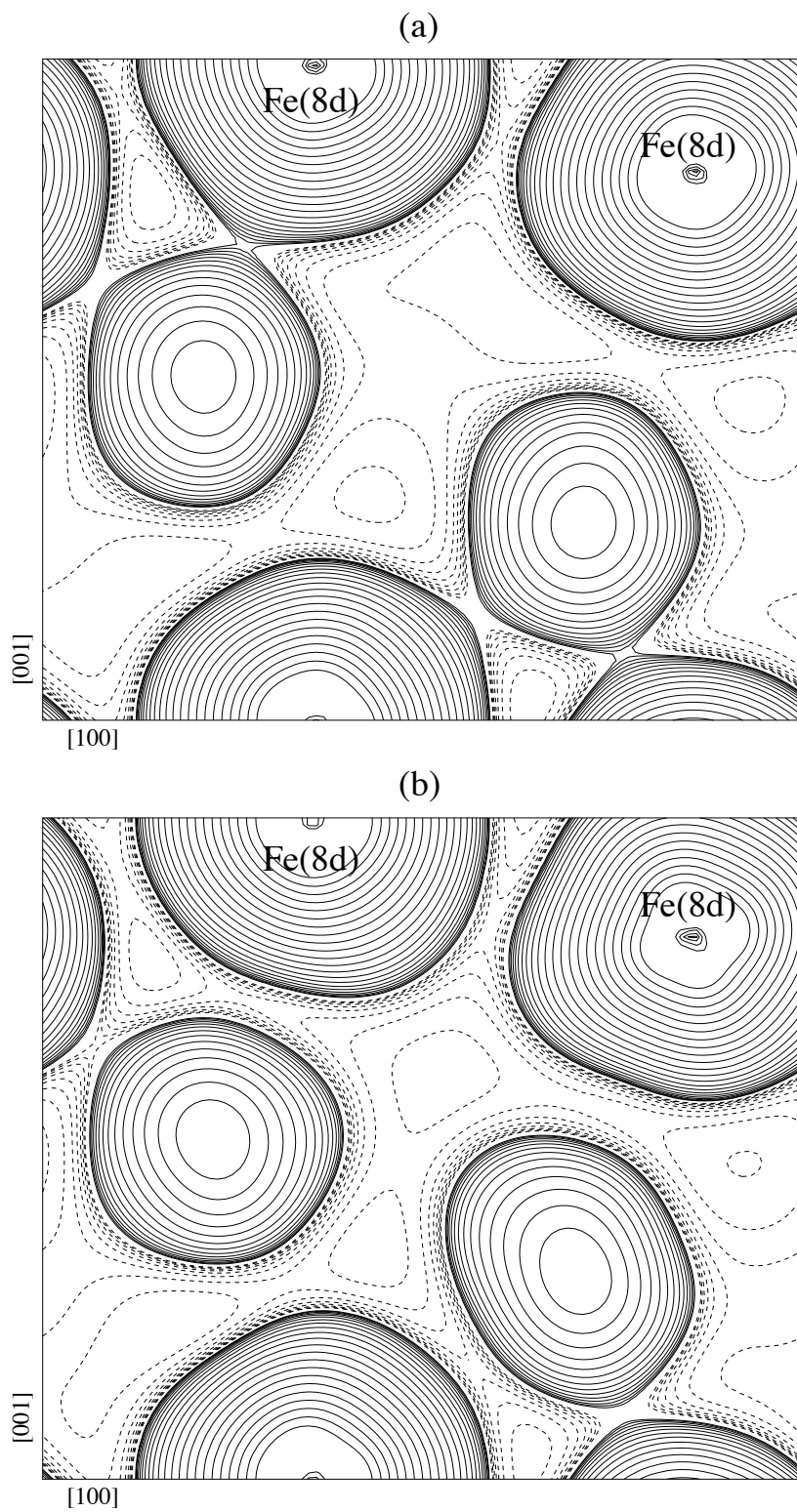


Fig. 6.

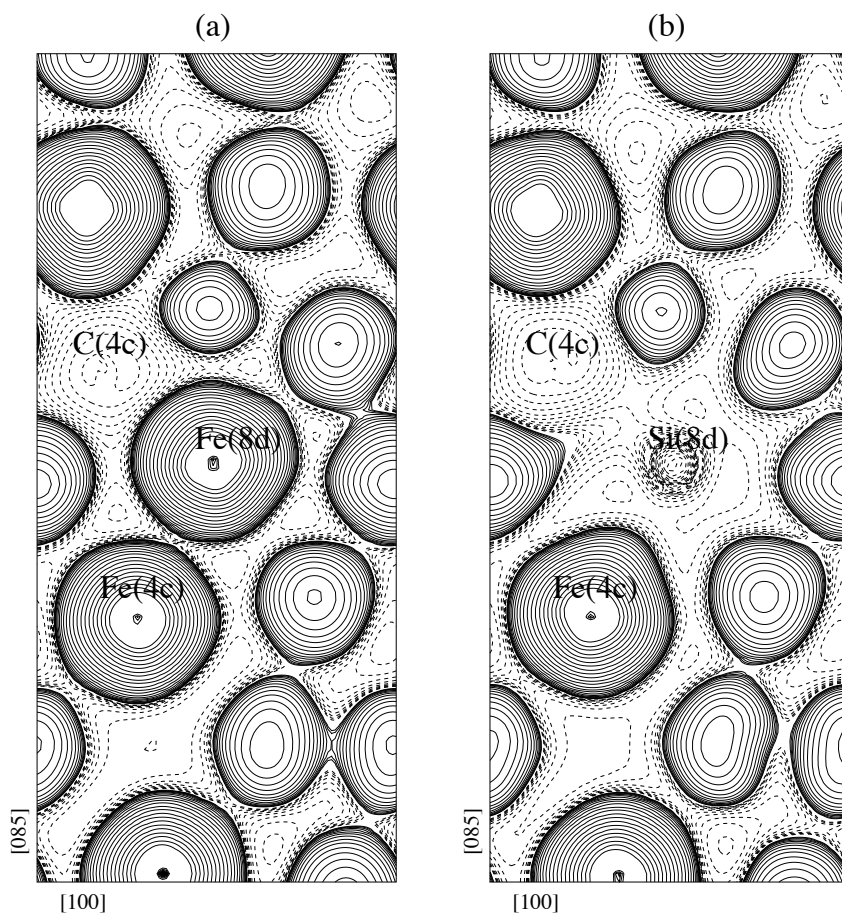


Fig. 7.

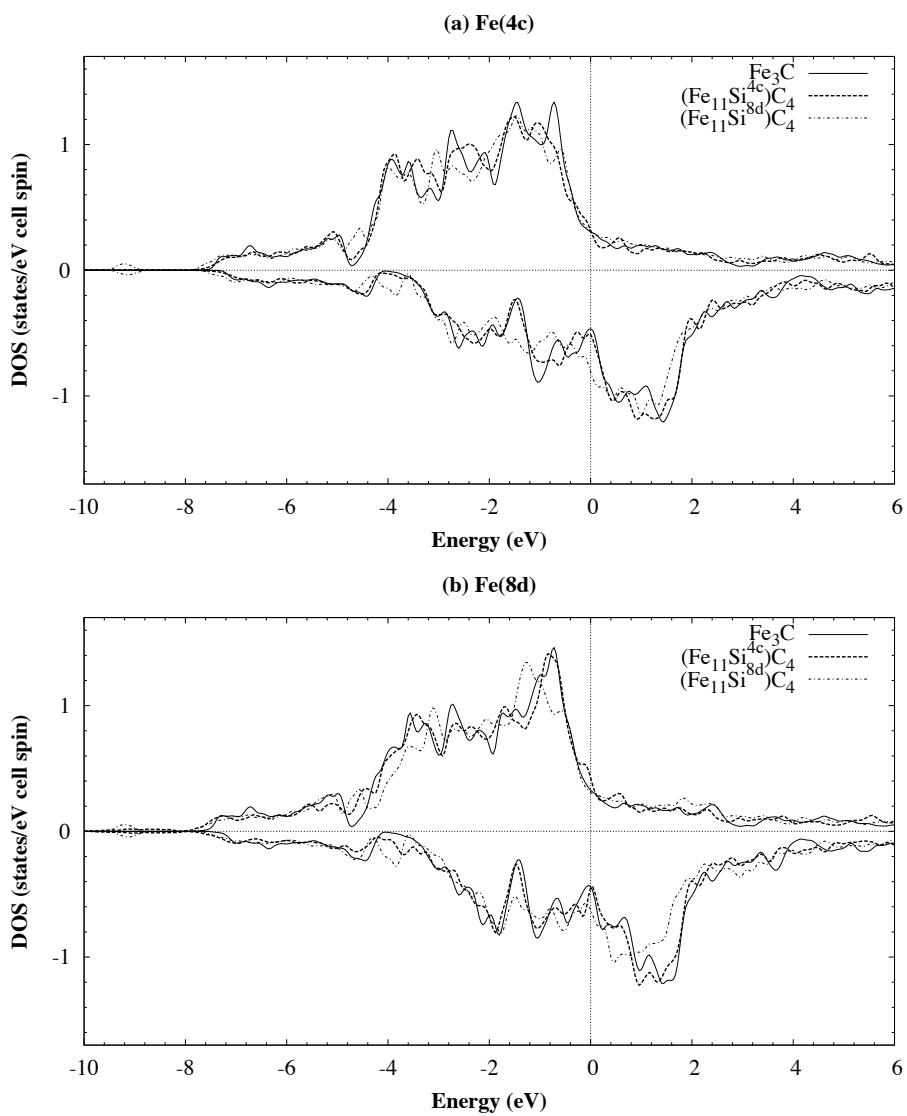


Fig. 8.